Highly ordered three-dimensional Ni-TiO_2 nanoarrays as sodium ion battery anodes

Yang Xu,[†] Min Zhou,[†] Liaoyong Wen,[†] Chengliang Wang,[†] Huaping Zhao,[†] Yan Mi,[†] Liying Liang,[†] Qun Fu,[‡] Minghong Wu,[‡] Yong Lei*[,†,‡]

[†]Institute of Physics & IMN MacroNano (ZIK), Technische Universität Ilmenau, Prof-Schemidt-Str. 26, 98693 Ilmenau, Germany. [‡]Institute of Nanochemistry and Nanobiology, School of Environment and Chemical Engineering, Shanghai University, 200444 P. R. China.

ABSTRACT: Sodium ion batteries (SIBs) represent an effective energy storage technology with potentially lower material costs than lithium ion batteries. Here we show that the electrochemical performance of SIBs, especially rate capability, is intimately connected to the electrode design at the nanoscale by taking anatase TiO_2 as an example. Highly ordered three-dimensional (3D) Ni-TiO_2 core-shell nanoarrays were fabricated using nanoimprited AAO templating technique and directly used as anode. The nanoarrays delivered a reversible capacity of ~200 mA h g^{-1} after 100 cycles at the current density of 50 mA h g^{-1} and were able to retain a capacity of ~95 mA h g^{-1} at the current density as high as 5 A g^{-1} and fully recover low rate capacity. High ion accessibility, fast electron transport, and excellent electrode integrity were shown as great merits to obtain the presented electrochemical performance. Our work demonstrates the possibility of highly ordered 3D heterostructured nanoarrays as a promising electrode design for Na energy storage to alleviate the reliance on the materials' intrinsic nature, and provides a versatile and cost-effective technique for the fabrication of such perfectly ordered nanostructures.

INTRODUCTION

Sodium ion batteries (SIBs) have attracted rapidly growing attention due to the low cost of Na associated with its natural abundance in both earth and ocean and decent energy density bestowed by its similar chemical nature to lithium.[1] Many electrode materials for lithium ion batteries (LIBs) have been investigated as drop-in replacement for SIBs because of the chemical similarity,[2-4] but their deficient intrinsic properties often lead to unsatisfactory battery performances or even complete electrochemical inactivity, for which the larger size of Na-ion relative to Li-ion is generally believed to be responsible.[5-7] This in turn motivates us to explore advanced electrode designs. Three-dimensional (3D) architecture featuring a periodic array of current collector and effective inclusion of active materials has been proven as a promising LIB electrode configuration to maximize power and energy density yet maintain short ion transport distance.[8-12] Unfortunately, so far little has been done on the end of SIBs regarding such 3D heterostructured electrode.[13] Due to the relatively large size of Na-ion, facile electron and ion transport as well as rigid electrode frame play a key role on improving electrochemical performance, especially rate capability, for a give material with intrinsically low electric conductivity. Highly ordered 3D metallic core/active shell nanoarrays can simultaneously offer sufficient electric conductivity and low ion diffusion resistance, as well as great electrode integrity deriving from the robust electric contact among the structural components. These advantages inspire us to apply this electrode design on SIBs.

To realize such heterostructured 3D nanoarrays, versatile and cost-effective techniques that can enable high regularity of nanounits are essentially needed. Anodic aluminum oxide (AAO) template-assisted methods constitute a powerful means to fabricate arrayed current collectors,[8-10,14] which subsequently can be used to obtain 3D electrodes with the incorporation of nanosized active materials. However, the lack of control on the structural parameters of the nanowire/nanorod arrays often leads to small inter-unit space, random orientation, and even the formation of the agglomerated clusters,[15] which results in the increase of supplementary interface between active materials, the block of ion flow, and the decrease of a surface area, thus deteriorating the rate capability.[8] As we mentioned, a highly ordered current collector array with sufficient inter-unit space is extremely desirable to ensure high ion accessibility. Nanoimprinted AAO technique has been previously used by our group to fabricate perfectly ordered nanopore and nanoparticle arrays.[16-18] The technique can provide high regularity of nanounits and sufficient inter-unit space, and the structural parameters of nanounits, such as size, length, interspace, can be precisely tuned through template fabrication. Meanwhile, the technique doesn't require complex and expensive facilities, tedious preparation and implementation steps. Therefore, we seek to use this versatile and cost-effective technique to construct a 3D nanoarrays electrode with a metallic core/active material shell nanostructure. Again, such architecture can simultaneously offer fast electron transport, high ion accessibility, and excellent electrode integrity (Figure 1), which is essential to improve rate capability of SIBs.

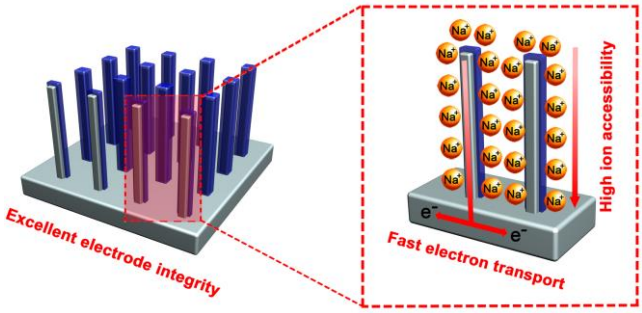

Figure 1. Schematic illustration of the highly ordered 3D electrode configuration with arrayed current collector, highlighting the fast electron transport, high ion accessibility, and excellent electrode integrity.

The material selected to demonstrate the concept of the highly ordered 3D nanoarrays is anatase TiO_2 (a-TiO_2, hereafter). Due to the exceptional stability, nontoxicity, low cost and abundance, TiO_2 has attracted considerable interests since the first report of it as a potential anode material for SIBs.[19] A few TiO_2 polymorphs are able to accommodate Na-ion into their structures,[20-22] with a-TiO_2 being the most studied so far.[22-29] Much effort has been devoted to improving the rate capability of a-TiO_2-based SIBs by incorporating carbonaceous materials as either conductive additive or coating layers in the conventional two-dimensional (2D) slurry electrode configuration.[23,26,28] In this work, highly ordered 3D Ni-TiO_2 nanoarrays (NTNAs, hereafter) were successfully fabricated by combining nanoimprinted AAO templates and atomic layer deposition (ALD). The 3D conductive network consisting of Ni nanopillar arrays and Ni current-carrying substrate serves the component to facilitate effective electron transport and the structural support, and the high regularity of the nanopillars with sufficient interspace provides high Na-ion accessibility. As expect, the NTNAs, used as conductive additive- and binder-free anodes, showed long-term cycling stability with a reversible capacity of ~200 mA h g^{-1} after 100 cycles. More importantly, the anode exhibited the rate capability of retaining a capacity of ~95 mA h g^{-1} at the current density as high as 5 A g^{-1} and fully recovering low rate capacity. Our study moves Ti-based anode design from 2D to 3D and highlights the positive effect of such nanoengineering on rate capability of SIBs. We believe the results can potentially arouse further attention on developing advanced electrode designs of SIBs regarding the active materials with deficient intrinsic properties.

RESULTS AND DISCUSSION

Figure 2a demonstrates the schematics of the fabrication process of the highly ordered 3D NTNAs. Starting from the imprinting of Al foil using a Ni stamp that has the perfect arrays of pyramid tips in a square lattice with the periodic distance of 400 nm, the imprinted Al foil was then subjected to anodization to form perfectly ordered square-shaped nanopore arrays (step A). Electrochemical deposition of a thick Ni layer, as the current-carrying substrate, was performed, followed by a subsequent pore-opening process by ion milling to obtain a through-pore AAO template (step B). Afterwards, electrochemical deposition of Ni nanopillars inside the square-shaped pores and the subsequent removal of the template (dissolved in a 5 wt% H_3PO_4 solution at 30°C) led to a 3D conductive network consisting of the current-collecting arrays and current-carrying substrate (step C). A 40 nm thick layer of TiO_2 was then uniformly coated on the nanopillar surfaces together with a post-annealing treatment to finally obtain the highly ordered 3D NTNAs (step D). Figure 2b and e show the representative scanning electron microscope (SEM) images of the as-prepared AAO template with square-shaped pores with a size of ~150 nm and pore depth of 1.2-1.3 μm. The images clearly demonstrate the long-range and perfect ordering of the pore arrays. The Ni nanopillar arrays faithfully reproduced the perfect order that derives from the high regularity of the template after the electrochemical deposition and template removal (Figure 2c). As shown in Figure 2f, the nanopillars vertically aligned and inherited the shape from the pore with a diameter of ~150 nm, and the rough surface is very likely due to the polycrystallined nature of Ni, which is commonly observed from the electrochemically deposited metal nanostructures. Figure 2d and g show the uniform coating of TiO_2 on the surfaces of the Ni nanopillars, increasing the diameter from ~150 to ~230 nm. Again, the high regularity and ordered arrangement were perfectly preserved after post-annealing treatment to enhance the crystallinity of TiO_2. No agglomeration between the nanopillars or collapse of the vertical alignment was observed, firmly confirming the successful realization of the highly ordered 3D NTNAs.

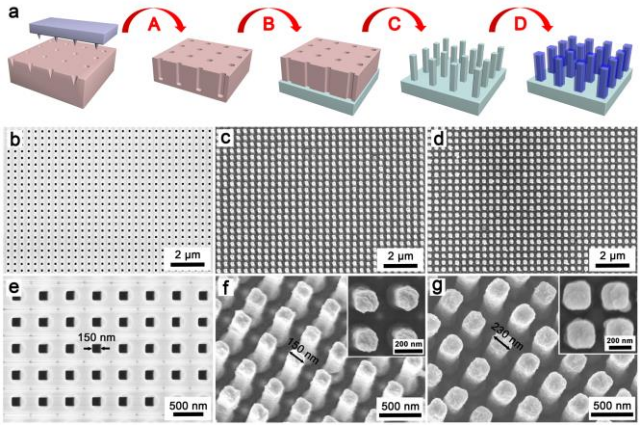

Figure 2. (a) Schematic illustration of the fabrication of the highly ordered 3D NTNAs using nanoimprinted AAO templating technique: (step A) anodization of pre-patterned Al foil; (step B) electrochemical deposition of Ni current-carrying substrate and removal of backside Al and barrier layer; (step C) electrochemical deposition of Ni nanopillar arrays and removal of AAO; (step D) ALD deposition of TiO_2 and post-annealing treatment. SEM images of the AAO template (b and e), Ni nanopillar arrays (c and f), and 3D NTNAs (d and g). Insets in (f) and (g) are the corresponding top-view images.

The phase and purity of the as-prepared 3D NTNAs were examined by X-ray diffraction (XRD). Due to the high intensity of the diffraction peaks from Ni and Au (Figure 3a), the lower intensity range is enlarged as shown in Figure 3b. Except for the diffraction peaks of Ni (JCPDS No. 65-2865) and Au (JCPDS No. 65-8601), all the other peaks can be indexed to (101), (200), (105)/(211), and (204) diffractions of the tetragonal a-TiO_2 (JCPDS No. 21-1272). No peaks from other phases can be detected, indicating the high purity of the as-prepared nanopillar arrays. Transmission electron microscopy (TEM) analysis was conducted by scratching the nanopillars off the current-carrying substrate and dispersing them in ethanol followed by ultrasonication. The elemental distribution across the nanopillar was investigated by energy-dispersive X-ray spectroscopy (EDX) line scan and verifies the presence of Ti, Ni, and O (Figure 3c). The elemental distribution of Ti

shows two peaks located at the wall position of the nanopillar, whereas Ni is distributed uniformly across the nanopillar, indicating its conformal core-shell structure. Figure 3d shows that the nanopillar has a uniform diameter of ~230 nm along its length, which is in agreement with the results from SEM analysis. The strong contrast between the inner and outer part further confirms the successful coating of TiO_2. Selected area electron diffraction (SAED) pattern shows well-defined concentric diffraction rings associated with a-TiO_2, where the first five concentric rings from the center can be indexed to (101), (200), (004), (105)/(211), and (204) planes in order. The diffraction rings are in agreement with the XRD results (the (004) peak (2θ=37.8°) is overlapped with the Au (111) peak (2θ=38.2°)). The HRTEM image (Figure 3e) clearly shows the lattice spacing of 3.5 Å corresponding to the separations between (101) plane, further confirming the high crystallinity of the sample. Summarizing the images and chemical analysis, we have successfully fabricated the highly ordered 3D NTNAs where a 3D conductive network is formed by the vertically aligned Ni nanopillars standing on the Ni current-carrying substrate, and uniformly coated a-TiO_2 acts as active material.

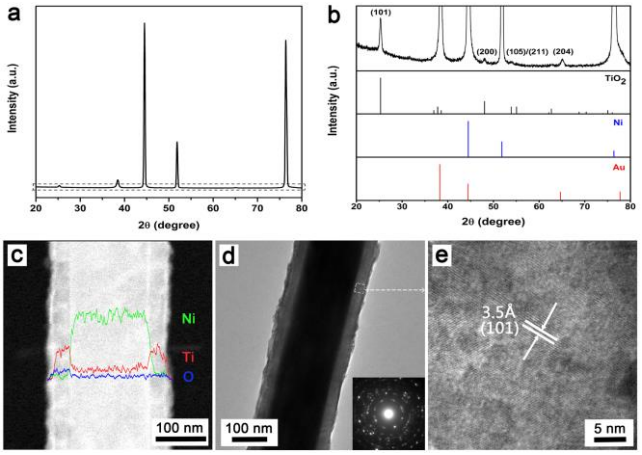

Figure 3. (a and b) XRD pattern of the 3D NTNAs. (c) Dark field TEM image of a single nanopillar with EDX line scan showing the elemental distribution of Ni, Ti, and O across the nanopillar. (d) Bright field TEM image of a single nanopillar (inset: SAED pattern). (e) HRTEM image recorded at the rectangular area in (d).

The Na-ion insertion/extraction behavior of the 3D NTNAs anode was investigated by cyclic voltammetry (CV). Figure 4 shows the CV curves of the first 15 cycles at a scan rate of 0.5 mV s^{-1} in the potential range of 0.01-2.5 V (*vs.* Na/Na^+). During the first cathodic scan, the broad peak beginning at 0.9 V in a wide potential range with a peak position around 0.8 V is attributed to the decomposition of electrolyte, *i.e.* irreversible formation of the solid-electrolyte interphase (SEI).[22,23] The wide potential range of SEI formation close to the reversing potential is likely due to the considerably large surface area deriving from the arrayed structure. The origin of the peak at around 0.5 V is not fully clear. With respect to the subsequent cyclic sweeps, it might be that this peak does not disappear but shifts to higher potential, possibly caused by a reduced overpotential for the reversible Na storage. Similar phenomenon was also observed by a recent work.[23] While the anodic current is apparently increasing upon cycling, a new redox couple at 0.85 (anodic) and 0.65 V (cathodic) becomes pronounced, which indicates the reversible insertion/extraction of sodium, being in agreement with the previous works.[22,23,26,27] The continuous evolution of the redox couple is likely related to the kinetically hampered reversible sodiation/desodiation that requires some kind of activation.

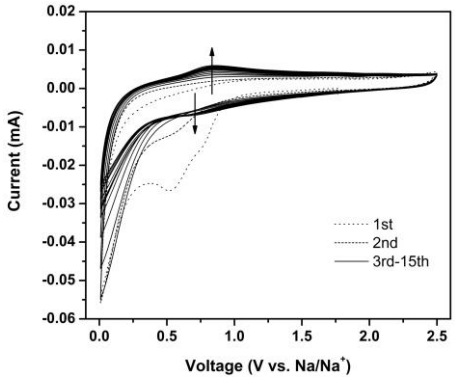

Figure 4. CV curves of the 3D NTNAs anode at a scan rate of 0.5 mV s^{-1} in the potential range of 0.01-2.5 V.

In order to demonstrate the critical roles of the arrayed current collector and its high regularity, we included two reference samples into the investigation of anode performance: (i) 3D close-ended TiO_2 nanotube arrays (TNAs, hereafter) that serve as the reference to show the effect of 3D conductive network. It is worth noting that close-ended nanotube arrays were chosen in order to obtain similar electrode/electrolyte contacting area with that of NTNAs, where the contacting area would be roughly doubled in the case of open-ended nanotube arrays; (ii) randomly-oriented Ni-TiO_2 core-shell nanopillar arrays (rNTNAs, hereafter) that serve as the reference to illustrate the importance of the high regularity. The crystal phase of both reference samples can be assigned to the tetragonal a-TiO_2 according to their XRD patterns (Figure S1). Both architectures have the similar structural parameters as 3D NTNAs. Shown in Figure 5a and c are 3D TNAs obtained by directly depositing TiO_2 inside the AAO template using ALD. The vertical alignment of the arrays can be clearly seen without the support from the Ni nanopillar arrays. The close-ended nanotubes possess a square-shaped cross section and a diameter of ~150 nm, both of which are inherited from the template. The thickness of 40 nm and hollow center can be confirmed from the TEM image (Figure S2). 3D rNTNAs were obtained by employing the randomly-oriented Ni nanopillar arrays as current collector followed by the ALD deposition of TiO_2 with the same thickness. Due to the attachment between the neighboring Ni nanopillars (Figure S3), severe agglomeration was observed after TiO_2 coating (Figure 5b and d), leading to the loss of the perfect alignment and less contact area between TiO_2 and electrolyte. Here, we chose the above two references to verify the improvement of electrochemical performance, especially that of rate capability, because of fast electron transport and high accessibility.

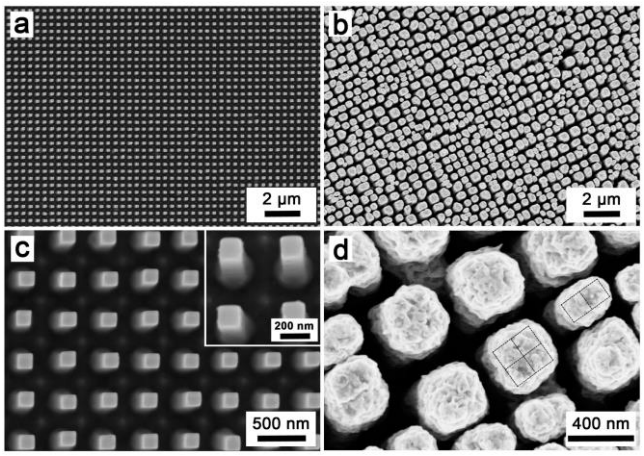

Figure 5. SEM images of the 3D TNAs (a and c) and rNTNAs (b and d). The dashed rectangles in (d) indicate the number of the attached nanopillars.

Figure 6a compares the cycling performance of the three nanoarrays directly employed as SIB anodes without any conductive additive and binder, and the cycling performance were investigated by galvanostatic charge and discharge between 0.01 and 2.5 V (*vs.* Na/Na^+) at the current density of 50 mA g^{-1}. The first discharge capacities are ~600, 550, and 400 mA h g^{-1} for 3D NTNAs, rNTNAs, and TNAs anode, respectively, with rather low initial columbic efficiency (CE), which is associated with the formation of the SEI layer that is related to the large surface area deriving from the arrayed structures. Analysis of the capacity and CE of the subsequent cycles allows us to draw the following conclusions. (i) Upon the introduction of 3D conductive network, both reversible Na storage and CE are significantly improved across the entire cycling process due to the faster electron transport between the active redox sites on a-TiO_2, current-collecting arrays, and current-carrying substrate. As shown in Figure 6b, TNAs anode exhibited rapidly decreased discharge capacity within the initial few cycles and reached a stabilized value of ~120 mA h g^{-1} afterwards. Both reversible capacity and CE are lower than those of NTNAs and rNTNAs anodes. The two core-shell arrayed anodes delivered increased discharge capacity of 292 (2nd) and 218 mA h g^{-1} (50th) for NTNAs, and 242 (2nd) and 187 mA h g^{-1} (50th) for rNTNAs (Figure 6b), respectively, as well as improved CE. With the existence of the 3D conductive network, the coated TiO_2 on each nanopillar has its "own" current collector and electrons from redox sites diffuse a short horizontal path (less than the thickness of a-TiO_2 layer) within the solid before reaching the current collector, thus diffusion resistance is largely reduced. In contrast, in the case of TNAs, electrons from redox sites need to diffuse along the longitude direction through a distance that can be as much as the length of nanopillars to reach the bottom current-carrying substrate. Significantly increased diffusion resistance exists due to the low intrinsic electric conductivity of a-TiO_2 comparing with NTNAs and rNTNAs anodes. (ii) The vertical alignment of nanopillars effectively ensures the highway diffusion of Na^+ along the longitude direction and maintains the high surface area of the arrayed structure. Once the initially stabilized status has been established, NTNAs anode exhibited both increased reversible capacity (over 200 mA h g^{-1}) and CE (over 90% since the 18th cycle) comparing with rNTNAs anode. (iii) The robust electric contact among the structural components provides great integrity of NTNAs anode, giving rise to a discharge capacity of ~200 mA h g^{-1} after 100 cycles, which is among the best results regarding Ti-based SIB anodes.[19,23,28,30,31] Aside from the reversible capacity, voltage profiles reveal other details about the electrochemistry of sodiation/desodiation in the arrays host. The voltage profiles of the three arrays anodes are depicted in Figure 6c, d and e with cycle numbers labeled on individual curve. The long slope between 1.0 and 0.01 V with a plateau locating around 0.7-0.75 V is observed in the first discharge process, which is due to the continuous formation of SEI layer and in agreement with the CV curves. During the following cycles (2nd-10th), a broad and reversible discharging band in the range of 0.2-1.0 V and a charging band in the range of 0.6-1.2 V appear and represent the reversible sodiation and desodiation from a-TiO_2. In accordance with the activation process presented in Figure 4, a pronounced semi-plateau between 0.8-0.5 V is established after a few initial cycles and remains unchanged during the entire cycling process (Figure 6c). Same phenomenon is observed from rNTNAs (Figure 6d) and TNAs (Figure 6e) anodes too, but with slower establishing rate, resulting in their lower CE thereby demonstrating the benefits of the 3D conductive network in the electrode design.

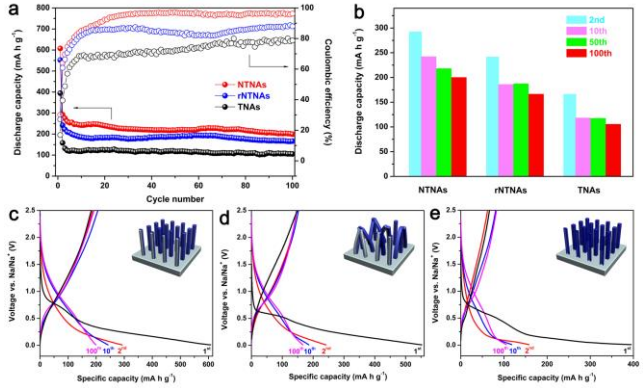

Figure 6. Cycling performance (a) and comparison of discharge capacity (b) of the three nanoarrays anodes. Discharge/charge profiles of the NTNAs (c), rNTNAs (d), and TNAs (e) anode at current density of 50 mA g^{-1}.

As mentioned previously, fast electron transport and high ion accessibility work synergistically to improve rate capability. Figure 7a compares the rate capability of the three arrays anodes with the current density ranging from 50 mA g^{-1} to 5 A g^{-1}. The capacity gradually decreases as the rate increases, and NTNAs anode provides higher Na storage capacity at all rates. It delivered the discharge capacities of 220, 192, 157, 132, and 110 mA h g^{-1} at the current density of 100, 200, 500, 1000, and 2000 mA g^{-1}. Even cycled at a current density as high as 5 A g^{-1}, a capacity of ~95 mA h g^{-1} can still be retained, whereas rNTNAs and TNAs anodes delivered the significantly lower capacities of ~63 and 23 mA h g^{-1}, respectively, under the same rate. Moreover, after cycling at high rates, a specific capacity of ~240 mA h g^{-1} can be obtained when the current density was reduced back to 50 mA g^{-1}, indicating a full recovery of the low rate capacity. As far as we know, the presented rate capability of the 3D NTNAs anode is comparable with the previously reported carbon-coated TiO_2 microspheres,[26] carbon-coated TiO_2 nanorods,[28] and TiO_2 nanoparticles,[23] and even better than TiO_2 nanoparticles/nitrogen-doped graphene composites.[27] However, it is worth emphasizing that the above reported capabilities were achieved by incorporating carbonaceous materials as either conductive additive or coat-

ing layer, whereas our electrode doesn't involve any kind of such materials, which clearly demonstrates the high dependence of electrochemical performance on purposely designed electrode configuration. The charge/discharge profiles of the NTNAs anode at different current density are shown in Figure 7b. As the rate increased, the discharge capacity progressively decreased, but with no significant voltage drop during the rate test. As shown in Figure 7c, fast electron transport and high ion accessibility can be simultaneously guaranteed for the 3D NTNAs anode by the 3D conductive network and vertical alignment of the nanopillars. Na ions reach the whole surface of TiO_2 layer through directly diffusing along the longitude direction between the nanopillars. At the same time, electrons from redox sites move through a distance of the thickness of TiO_2 layer to reach Ni pillars, thus being quickly collected by the 3D current collector. Although the rNTNAs anode possesses the 3D conductive network, the random orientation and/or attachment of the nanopillars reduce ion accessibility, which is crucial at high rates. On one hand, the attachment of nanopillars blocks the direct Na-ion diffusion path along the longitude direction such that Na-ions have to diffuse from outside of the nanopillar clusters to reach the inner surface of the TiO_2 layer, giving rise to higher Na-ion diffusion resistance if considering the short time at high rates (~35 s for each charge or discharge process at the rate of 5 A g^{-1}). On the other hand, less Na-ions are accessible in the region with small size below the attached tips since the distance of closest approach to the surface depends on the size of the ion.[32] A recent work showed that noteworthy intercalation of Na-ions cannot be observed when cycling TiO_2 nanotubes with the diameter less than 45 nm,[19] therefore, enough space is necessary to transport ions to TiO_2 surface. The opposite situation happens to the TNAs anode. The vertical alignment of the nanotubes provides direct Na-ion diffusion path along the longitude direction to reach the whole surface of the TiO_2 layer. But longer electron diffusion paths than those in the case of NTNAs exist when electrons transport from active redox sites to the film current collector at the bottom of the electrode. Longer diffusion paths lead to higher diffusion resistance due to the low intrinsic electric conductivity of anatase TiO_2, resulting in low capacity at high rates. The comparison here shows that both high ion accessibility and fast electron transport deriving from the purposely designed electrode configuration are essential to reach great rate capability.

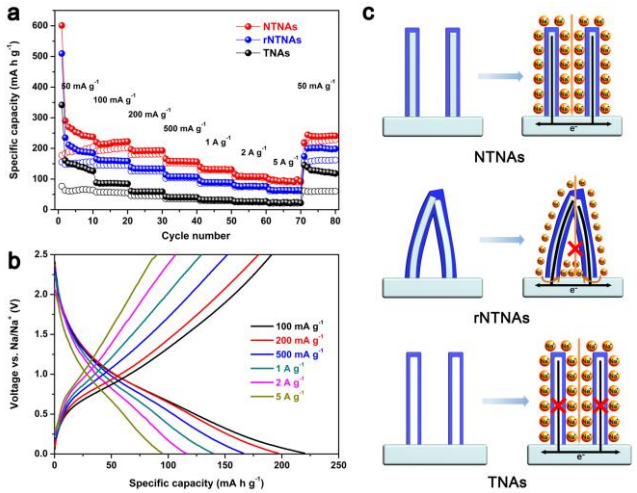

Figure 7. (a) Rate capability of the three nanoarrays anodes. (b) Discharge/charge profiles of the 3D NTNAs anode at elevated rates. (c) Schematic illustration of the comparison regarding electron transport and ion accessibility for the three nanoarrays anodes during discharge/charge process.

With the above electrochemical performance presented, we next seek to observe how the electrode integrity behaves upon repeated discharge/charge process. We have pointed out that excellent electrode integrity originates from the robust electric contact among the structural components, which inspires us to examine the resistance of the arrays to gain insight into the electron transport within the matrix and the electric contact with the current collector. As shown in Figure 8a, the resulting symmetric and linear appearance indicates the Ohmic contact between the coating layer and arrayed current collector, and the smaller resistance of the NTNAs than that of the TNAs by one order of magnitude results in much better electron transport. Electrochemical impedance spectroscopy (EIS) measurements were carried out on the two anodes after cycling at different rate steps (Figure S4). The substantially smaller radii of the depressed semicircles at each testing rate imply the much smaller charge transfer resistance of NTNAs than that of TNAs, verifying the improved rate capability shown in Figure 7a. In addition, post-cycling examination further gives us visual understanding. Shown in Figure 8b and S5 are the SEM images of the NTNAs anode collected after 100 discharge/charge cycles, from which it can be seen that the vertical alignment of the nanopillars was completely preserved on the current-carrying substrate. The diameter of the pillars increased likely due to the continuous formation of the SEI layer during the initial cycles, which was previously discussed regarding the CV and discharge/charge results. Nevertheless, no collapse of the arrayed structure or attachment between neighboring nanopillar can be observed, demonstrating the great electrode integrity upon long-term cycling. In return, it further solidifies the conclusion that both fast electron transport and high ion accessibility can be guaranteed on the basis of the strong structural stability. It is worth mentioning that there still is room to further improve the electrochemical performances by optimizing the TiO_2-coating thickness (Figure S6) and interunit distance through AAO template fabrication. Particularly regarding the latter, a continuing study is currently under investigation. Nevertheless, the reported anode performance falls in a desirable range. Further increase of the anode capacity should collaboratively contribute to the overall cell capacity improvement with breakthroughs in increasing the capacities of SIB cathode by, for example, other advanced electrode designs, and the electrolyte.[1]

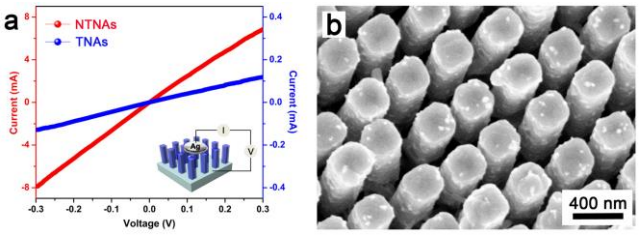

Figure 8. (a) Current-voltage (I-V) characteristics with a schematic view of the nanoarrays anode. (b) SEM image of the 3D NTNAs anode after 100 cycles at a current density of 50 mA g^{-1}.

CONCLUSION

In summary, we have synthesized highly ordered 3D Ni-TiO_2 core-shell nanopillar arrays consisting of anatase TiO_2 outer layer, Ni nanopillar current-collecting arrays, and Ni current-

carrying substrate by combining the nanoimprinted AAO templating technique and ALD. The heterostructured nanoarrays were directly employed as anodes and demonstrated good electrochemical performance, especially rate capability, toward Na-ion storage and release. It delivered a capacity of ~260 mA h g^{-1} in the initial cycles and retained ~200 mA h g^{-1} after 100 cycles, and a capacity of ~95 mA h g^{-1} at the current density as high as 5 A g^{-1} with fully recovering the low rate capacity. The vertical alignment of nanopillars and the 3D conductive network were believed to function synergistically to maintain high ion accessibility and fast electron transport as well as excellent electrode integrity during fast charge/discharge process. The essence of the 3D electrode configuration is realized by the nanoimprinted AAO templating technique that can be possibly used for other advanced electrode designs regarding other extensively studied materials for Na energy storage, such as SnO_2[33] and other transition metal oxides.[34,35]

EXPERIMENTAL SECTION

Preparation of the AAO template: AAO template was prepared using nanoimprinting technique followed by an anodization process. Aluminum foil with a purity of 99.99% was electrochemically polished in a mixture solution of perchloric acid and ethanol (1:7, v:v) at a voltage of 30 V. The Ni imprinting stamp was placed on top of the polished Al foil, and the imprinted Al foil was obtained by applying a pressure of about 10 kN cm^{-2} for 3 min using an oil pressing system. The anodization of the imprinted Al foil was conducted under a constant voltage of 160 V in a H_3PO_4 solution (0.2 M) at 2°C for 2 h, where the anodization voltage was chosen to match the periodic distance in the imprinting stamp due to the linear relationship (2.5 nm V^{-1}) between the inter-pore distance (400 nm) and anodization potential (160 V). Afterwards, a thick layer of Ni was electrochemically deposited on top of the AAO template as current-carrying substrate, before which a 30 nm thick layer of Au was evaporated by physical vapor deposition (PVD) to improve the adhesion between Ni layer and template. The remaining backside Al was removed by a mixture solution of $CuCl_2$ solution (3.4 g in 100 ml H_2O) and HCl (100 ml). Then, the barrier layer was removed by ion milling to form a through-pore AAO template.

Fabrication of the 3D Ni nanopillar arrays: 3D Ni nanopillar arrays were electrochemically deposited in Watt's bath as electrolyte, which consists of $NiSO_4 \cdot 6H_2O$ (0.38 M), $NiCl_2 \cdot 6H_2O$ (0.12 M), and H_3BO_3 (0.5 M). Two-electrode configuration was used with the as-prepared through-pore AAO template as working electrode and Ni foil as counter electrode. The electrochemical deposition was performed by constant current mode using a VSP electrochemical workstation (Bio-Logic, France), where a current of -2 mA was applied for 7 minutes. Afterwards, the AAO template was removed in a 5 wt% H_3PO_4 solution at 30°C.

Fabrication of the 3D NTNAs: the 3D NTNAs were fabricated by depositing a 40 nm thick layer of TiO_2 on the surface of the as-prepared Ni nanopillar arrays using a PicoSun SUNALE™ R-150 ALD system (PicoSun, Finland) according to the following procedure. The reaction chamber was heated to 300°C, and $TiCl_4$ and H_2O were chosen as the precursors of Ti and O, respectively. $TiCl_4$ was pulsed for 0.1 s and purged for 10 s, followed by a 0.1 s pulse and 10 s purge of H_2O. This procedure was repeated for 800 times according to the growth rate of ~0.5 Å per cycle to reach a thickness of 40 nm. The as-prepared arrays were annealed in air at 350°C for 2 h with a ramp rate of 2°C/min. For comparison, 3D TNAs and rNTNAs were also fabricated using the similar procedures.

Characterization: X-ray diffraction (XRD) analysis was performed on a SIEMENS/BRUKER D5000 X-ray diffractometer using Cu-Kα radiation at 40 kV and 40 mA, with the samples being scanned from 2θ = 20°-80° at rate of 0.02° s^{-1} in a Bragg-Brentano geometry. Scanning electron microscopy (SEM) analysis was conducted using a Hitachi S4800 field emission scanning microscopy. Transmission electron microscopy (TEM) analysis was performed on a Philips Tecnai™ transmission electron microscope. I-V characterization was performed on VSP electrochemical workstation (Bio-Logic, France).

Electrochemical measurement: the as-prepared 3D nanoarrays were directly used as an anode without adding conductive additive and polymeric binder. Electrochemical tests were carried out using a coin cell configuration, CR2032, with a diameter and thickness of 20 mm and 3.2 mm, respectively, which were assembled in a nitrogen-filled glove box with oxygen and moisture concentrations kept below 0.1 ppm. Sodium metal foil used as a counter electrode was separated from the working electrode using a glass microfiber filter (Whatman, Grade GF/B) with the pore size of 1 μm. The electrolyte was 1 M sodium perchlorate ($NaClO_4$) salt in propylene carbonate (PC, Aldrich anhydrous 99.7%). Cyclic voltammetry (CV) was performed on a VSP electrochemical workstation (Bio-Logic, France) with a scan rate of 0.5 mV s^{-1} in the potential range of 0.01 to 2.5 V (*vs.* Na/Na^+). Electrochemical impedance spectroscopy (EIS) was performed on the same workstation with a frequency range of 10^6-10^{-2} Hz and a 5 mV AC amplitude. Galvanostatic discharge/charge was carried out on a Land CT2001A battery testing system (Land, P. R. China) with the cutoff potentials set to 0.01-2.5 V (*vs.* Na/Na^+) at room temperature.

ASSOCIATED CONTENT

Supporting Information: the XRD patterns of rNTNAs and TNAs, TEM image of a single close-ended TiO_2 nanotube, SEM images of the attached Ni nanopillar arrays, Nyquist plots of the NTNAs and TNAs anodes after cycling at different rate steps, low-magnification SEM image of the 3D NTNAs anode after 100 cycles at the current density of 50 mA g^{-1}, and rate capability and cycling performance at the current density of 200 mA g^{-1} of the NTNAs anode with a TiO_2 thickness of 20 nm. This material is available free of charge via the Internet at http://pubs.acs.org.

AUTHOR INFORMATION

Corresponding Author

* yong.lei@tu-ilmenau.de

ACKNOWLEDGMENT

This work was financially supported by the European Research Council (ThreeDsurface: 240144), BMBF (ZIK-3DNanoDevice: 03Z1MN11), Volkswagen-Stiftung (Herstellung funktionaler Oberflächen: I/83 984), Shanghai Thousand Talent and Program, and Innovative Research Team in University (No. IRT13078). We thank Mr. Yong Yan for his assistance with XRD measurement.

REFERENCES

(1) Yabuuchi, N.; Kubota, K.; Dahbi, M.; Komaba, S. Research Development on Sodium-Ion Batteries. *Chem. Rev.* **2014**, *114*, 11636.

(2) Palomares, V.; Serras, P.; Villaluenga, I.; Hueso, K.; Carretero-González, J.; Rojo, T. Na-Ion Batteries, Recent Advances and Present Challenges to Become Low Cost Energy Storage Systems. *Energy Environ. Sci.* **2012**, *5*, 5884.

(3) Slater, M.; Kim, D.; Lee, E.; Johnson, C. Sodium-Ion Batteries. *Adv. Funct. Mater.* **2013**, *23*, 947.

(4) Pan, H.; Hu, Y.; Chen, L. Room-Temperature Stationary Sodium-Ion Batteries for Large-Scale Electric Energy Storage. *Energy Environ. Sci.* **2013**, *6*, 2338.

(5) Ong, S.; Chevrier, V.; Hautier, G.; Jain, A.; Moore, C.; Kim, S.; Ma, X.; Ceder, G. Voltage, Stability and Diffusion Barrier Differences Between Sodium-Ion and Lithium-Ion Intercalation Materials. *Energy Environ. Sci.* **2011**, *4*, 3680.

(6) Chevrier, V.; Ceder, G. Challenges for Na-Ion Negative Electrodes. *J. Electrochem. Soc.* **2011**, *158*, A1011.

(7) Klein, F.; Jache, B.; Bhide, A.; Adelhelm, P. Conversion Reaction for Sodium-Ion Batteries. *Phys. Chem. Chem. Phys.* **2013**, *15*, 15876.

(8) Taberna, P.; Mitra, S.; Poizot, P.; Simon, P.; Tarascon, J. High Rate Capabilities Fe_3O_4-Based Cu Nano-Architectured Electrodes for Lithium-Ion Battery Applications. *Nat. Mater.* **2006**, *5*, 567.

(9) Cheah, S.; Perre, E.; Rooth, M.; Fondell, M.; Hårsta, A.; Nyholm, L.; Boman, M.; Gustafsson, T.; Lu, J.; Simon, P.; Edström, K. Nanoelectrodes for Microbattery Applications. *Nano Lett.* **2009**, *9*, 3230.

(10) Shaijumon, M.; Perre, E.; Daffos, B.; Taberna, P.; Tarascon, J.; Simon, P. Nanoarchitectured 3D Cathodes for Li-Ion Microbatteries. *Adv. Mater.* **2010**, *22*, 4978.

(11) Cao, F.; Deng, J.; Xin, S.; Ji, H.; Schmidt, O.; Wan, L.; Guo, Y. Cu-Si Nanocable Arrays as High-Rate Anode Materials for Lithium-Ion Batteries. *Adv. Mater.* **2011**, *23*, 4415.

(12) Liu, Y.; Zhang, W.; Zhu, Y.; Luo, Y.; Xu, Y.; Brown, A.; Culver, J.; Lundgren, C.; Xu, K.; Wang, Y.; Wang, C. Architecturing Hiearchical Function Layers on Self-Assembled Viral Templates as 3D Nano-Array Electrodes for Integrated Li-Ion Microbatteries. *Nano Lett.* **2013**, *13*, 293.

(13) Liu, Y.; Xu, Y.; Zhu, Y.; Culver, J.; Lundgren, C.; Xu, K.; Wang, C. Tin-Coated Viral Nanoforests as Sodium-Ion Battery Anodes. *ACS Nano* **2013**, *7*, 3627.

(14) Perre, E.; Nyholm, L.; Gustafsson, T.; Taberna, P.; Simon, P.; Edström, K. Direct Electrodeposition of Aluminium Nano-Rods. *Electrochem. Commun.* **2008**, *10*, 1467.

(15) Dangwal, A.; Pandey, C.; Müller, G.; Karim, S.; Cornelius, T.; Trautmann, C. Field Emission Properties of Electrochemically Deposited Gold Nanowires. *Appl. Phys. Lett.* **2008**, *92*, 063115.

(16) Zhan, Z.; Lei, Y. Sub-100-nm Nanoparticles Arrays with Perfect Ordering, Tunable and Uniform Dimensions Fabricated by Combing Nanoimprinting with Ultrathin Alumina Membrane Technique. *ACS Nano*, **2014**, *8*, 3862.

(17) Wen, L.; Mi, Y.; Wang, C.; Fang, Y.; Grote, F.; Zhao, H.; Zhou, M.; Lei, Y. Cost-Effective Atomic Layer Deposition Synthesis of Pt Nanotube Arrays: Application for High Performance Supercapacitor. *Small* **2014**, *10*, 3162.

(18) Zhao, H.; Wang, C.; Vellacheri, R.; Zhou, M.; Xu, Y.; Fu, Q.; Wu, M.; Grote, F.; Lei, Y. Self-Supported Metallic Nanopores Arrays with Highly-Ordered Nanoporous Structure as Ideally Nanostructured Electrode for Supercapacitor Application. *Adv. Mater.* **2014**, *26*, 7654.

(19) Xiong, H.; Slater, M.; Balasubramanian, M.; Johnson, C.; Rajh, T. Amorphous TiO_2 Nanotube Anode for Rechargeable Sodium Ion Batteries. *J. Phys. Chem. Lett.* **2011**, *2*, 2560.

(20) Pérez-Flores, J.; Baehtz, C.; Kuhn, A.; García-Alvarado, F. Hollandite-Type TiO_2: A New Negative Electrode Material for Sodium-Ion Batteries. *J. Mater. Chem. A* **2014**, *2*, 1825.

(21) Huang, J.; Yuan, D.; Zhang, Z.; Cao, Y.; Li, G.; Yang, H.; Gao, X. Electrochemical Sodium Storage of TiO_2(B) Nanotubes for Sodium Ion Batteries. *RSC Advances* **2013**, *3*, 12593.

(22) Xu, Y.; Lotfabad, E.; Wang, H.; Farbod, B.; Xu, Z.; Kohandehghan, A.; Mitlin, D. Nanocrystalline Anatase TiO_2: A New Anode Material for Rechargeable Sodium Ion Batteries. *Chem. Commun.* **2013**, *49*, 8973.

(23) Wu, L.; Buchholz, D.; Bresser, D.; Chagas, L.; Passerini, S. Anatase TiO_2 Nanoparticles for High Power Sodium-Ion Anodes. *J. Power Sources* **2014**, *251*, 379.

(24) González, J.; Alcántara, R.; Nacimiento, F.; Ortiz, G.; Tirado, J. Microstructure of the Epitaxial Film of Anatase Nanotubes Obtained at High Voltage and the Mechanism of Its Electrochemical Reaction with Sodium. *CrystEngComm* **2014**, *16*, 4602.

(25) Wu, L.; Bresser, D.; Buchholz, D.; Giffin, G.; Castro, C.; Ochel, A.; Passerini, S. Unfolding the Mechanism of Sodium Insertion in Anatase TiO_2 Nanoparticles. *Adv. Energy Mater.* **2014**, DOI: 10.1002/aenm.201401142.

(26) Oh, S.; Hwang, J.; Yoon, C.; Lu, J.; Amine, K.; Belharouak, I.; Sun, Y. High Electrochemical Performances of Microsphere C-TiO_2 Anode for Sodium-Ion Battery. *ACS Appl. Mater. Interfaces* **2014**, *6*, 11295.

(27) Cha, H.; Jeong, H.; Kang, J. Nitrogen-Doped Open Pore Channeled Graphene Facilitating Electrochemical Performance of TiO_2 Nanoparticles as An Anode Material for Sodium Ion Batteries. *J. Mater. Chem. A* **2014**, *2*, 5182.

(28) Kim, K.; Ali, G.; Chung, K.; Yoon, C.; Yashiro, H.; Sun, Y.; Lu, J.; Amine, K.; Myung, S. Anatase Titania Nanorods as an Intercalation Anode Material for Rechargeable Sodium Batteries. *Nano Lett.* **2014**, *14*, 416.

(29) Dresser, D.; Oschmann, B.; Tahir, M.; Mueller, F.; Lieberwirth, I.; Tremel, W.; Zentel, R.; Passerini, S. Carbon-Coated Anatase TiO_2 Nanotubes for Li- and Na-Ion Anodes. *J. Electrochem. Soc.* **2015**, *162*, A3013.

(30) Rudola, A.; Saravanan, K.; Mason, C.; Balaya, P. $Na_2Ti_3O_7$: An Intercalation Based Anode for Sodium-Ion Battery Applications. *J. Mater. Chem. A* **2013**, *1*, 2653.

(31) Wang, W.; Yu, C.; Lin, Z.; Hou, J.; Zhu, H.; Jiao, S. Microshperic $Na_2Ti_3O_7$ Consisting of Tiny Nanotubes: An Anode Material for Sodium-Ion Batteries with Ultrafast Charge-Discharge Rate. *Nanoscale* **2013**, *5*, 594.

(32) Wynveen, A; Bresme, F. Properties of Alkali-Halide Salt Solutions About Polarizable Nanoparticles Solutes for Different Ion Modes. *J. Chem. Phys.* **2010**, *133*, 10.

(33) Su, D.; Ahn, H.; Wang, G. SnO2@Graphene Nanocomposites as Anode Materials for Na-Ion Batteries with Superior Electrochemical Performance. *Chem. Commun.* **2013**, *49*, 3131.

(34) Jiang, Y.; Hu, M.; Zhang, D.; Yuan, T.; Sun, W.; Xu, B.; Yan, M. Transition Metal Oxides for High Performance Sodium Ion Battery Anodes. *Nano Energy* **2014**, *5*, 60.

(35) Hariharan, S.; Saravanan, K.; Balaya, P. α-MoO_3: A High Performance Anode Material for Sodium-Ion Batteries. E*lectrochem. Commun.* **2013**, *31*, 5.